Ceramics International 48 (2022) 7730–7747

Contents lists available at ScienceDirect

Ceramics International

journal homepage: www.elsevier.com/locate/ceramint

Evaluation of pressure and temperature effect on the structure and properties of $Ca_{2.93}Sr_{0.07}Co_4O_9$ ceramic materials

M.A. Torres [a], M.A. Madre [a], O.J. Dura [b], G. García [c], S. Marinel [d], P. Martinez-Filgueira [c], A. Sotelo [a,*]

[a] Instituto de Nanociencia y Materiales de Aragón (INMA), CSIC-Universidad de Zaragoza, 50018, Zaragoza, Spain
[b] Departamento de Física Aplicada (Universidad de Castilla-La Mancha), 13071, Ciudad Real, Spain
[c] CS Centro Stirling S. Coop, Avda. Alava 3, 20550, Aretxabaleta, Spain
[d] Normandie Univ, ENSICAEN, UNICAEN, CNRS, CRISMAT, 14000, Caen, France

ARTICLE INFO

Keywords:
A. Hot pressing
C. Electrical properties
C. Mechanical properties
C. Thermal properties

ABSTRACT

In this work, the effect of hot-pressing conditions on the performances of Sr-doped $Ca_3Co_4O_9$ materials has been investigated. The samples were prepared from attrition milled precursors, which reduced the processing time. Samples were hot-pressed at temperatures (T) between 800 and 900 °C and pressures (P) from 51 to 71 MPa. The out-of-plane X-ray diffraction (XRD) showed that all samples are formed by the thermoelectric phase, with a good grain orientation which is improved with T, and P, as demonstrated by their Lotgering factor. The observations through Scanning Electron Microscopy (SEM) have revealed that grain sizes and orientation are enhanced with T, and P, as well as density through Archimedes's method. All these trends are reflected in the flexural strength and microhardness. The electrical resistivity is lower when the T, or P, is increased, reaching 6.4 mΩ cm for samples processed at 900 °C and 71 MPa, which is about the best reported values in the literature. On the other hand, contrarily to the expected results, they also showed the highest S values, 182 μV/K, which are similar to the best reported values for highly dense textured materials. Thermal conductivity values do not follow a regular evolution with the hot-pressing conditions, probably due to internal stresses, reaching the lowest values at 800 °C in samples processed at 800 °C and 51 MPa (1.51 W/(K*m)) or 900 °C and 61 MPa (1.53 W/(K*m)). Consequently, the highest ZT values have been determined in samples processed at 900 °C and 61 MPa (0.35) which is higher than the best reported values in literature for bulk textured samples, to the best of our knowledge.

1. . Introduction

Under the current situation on global warming, where most of the national governments are working and legislating for a more sustainable economy with less dependence on fossil fuels, thermoelectric materials can play an important role [1–3]. These materials are characterized by their ability to transform a temperature difference into electric power, without mobile parts, provided by the Seebeck effect. Consequently, these materials can be used to recover waste heat in many processes [4,5], or producing renewable energy from the sun [6]. On the other hand, the efficiency of such transformation can be quantified using a dimensionless magnitude called figure of merit, ZT, which can be calculated through the equation [7]:

$$ZT = \frac{S^2 T}{\rho \kappa} \quad \text{Eq. 1}$$

where S is the Seebeck coefficient, T the absolute temperature, ρ the electrical resistivity, and κ the total thermal conductivity. This expression clearly indicates that materials with high thermoelectric performances should show high Seebeck coefficient and low thermal conductivity and electric resistivity. Moreover, they have to be able to work at high temperatures, which results in higher efficiency. On the other hand, it is established that materials for practical applications should have ZT values ≥ 1.

Nowadays, some families display ZT values above 1, such as intermetallic compounds PbTe [8] or SnTe [9]. On the other hand, they are not able to work at elevated temperatures under air atmosphere due to possible oxidation or evaporation of heavy elements. Moreover, these

* Corresponding author. INMA, Maria de Luna, 3. 50018, Zaragoza, Spain.
E-mail address: asotelo@unizar.es (A. Sotelo).

https://doi.org/10.1016/j.ceramint.2021.11.321
Received 1 October 2021; Received in revised form 10 November 2021; Accepted 28 November 2021
Available online 1 December 2021

heavy constituents are scarce [10], expensive and, in most cases, hazardous to human health or the environment. These drawbacks have been surpassed when high thermoelectric properties were found in the $Na_2Co_2O_4$ ceramic materials [11]. This discovery pushed up the research on these ceramics which possess high chemical stability at high temperatures under air. Moreover, they are usually composed of more abundant and cheaper elements than the intermetallic ones [12]. Nowadays, some of the most promising CoO based materials for practical applications are $Ca_3Co_4O_x$ (also called 349) [13], and $Bi_2AE_2Co_2O_y$ (where AE is an Alkaline Earth metal) [14,15]. These CoO based materials share some crystallographic features, as they can be described through a monoclinic structure formed by the stacking of two different sublattices. The first one is a CoO_2 hexagonal conductive layer (CdI_2 type), and the second one with Rock Salt structure behaves as insulating layer, where the other cations are distributed [16]. Misfit cobaltites is the usual name used to describe materials due to the different b-axis length between both layers. This misfit factor can be manipulated by different techniques, leading to modifications of the Seebeck coefficient [17]. Another important characteristic of these materials is their anisotropy, with the most favorable direction for electrical conductivity along the preferential grain growth one. Consequently, this feature can be exploited to obtain low electrical resistivity materials, without significantly modifying Seebeck coefficient, by an optimal grain alignment with the ab-planes parallel to the electrical transport direction [18]. Many different methods have been shown to produce important grain alignment in these materials, which can be divided in processes through solid state, as the microwave sintering [19], hot-uniaxial pressing [20], spark plasma sintering (SPS) [21], or templated grain growth (TGG) [22]; and by transient liquid phase, as the laser floating zone (LFZ) [23], or the electrically assisted LFZ [24].

Taking into account these typical characteristics of cobaltite materials, the aim of this work is to study the effect of pressure and temperature on the structural, microstructural, electrical, thermal, and mechanical properties of hot uniaxially pressed and isovalently doped $Ca_3Co_4O_9$ ceramics prepared from attrition milled precursors. For this purpose, Sr substitution for Ca has been performed in order to modify the misfit factor without changing the charge of the Rock-Salt layer [25,26].

2. Experimental section

The nominal $Ca_{2.93}Sr_{0.07}Co_4O_9$ composition has been selected from previous works [27]. They were prepared using $CaCO_3$ (≥99%, Aldrich), $SrCO_3$ (≥98%, Aldrich), and CoO (99.99%, Aldrich) commercial powders in stoichiometric proportions. These powders were mixed and attrition milled in a self-made equipment rotating at 300 rpm, using 1 mm diameter ZrO_2 balls for 1 h in water media and a proportion balls: powder of 10:1, as previously reported [28]. The resulting suspension was then dried under infrared radiation and manually milled in an agate mortar to obtain an homogeneous fine powder mixture. The calcination of powders was performed at 850 °C for 1 h to completely decompose carbonates, as it has been previously demonstrated [29]. After a subsequent manual milling, the powders were uniaxially cold pressed in form of discs (25 mm diameter) under 250 MPa applied pressure. Finally, the green discs were subjected to a hot pressing process for 1 h under three different temperatures (800, 850, and 900 °C) and pressures (51, 61, and 71 MPa). The discs were subsequently cut into pieces for the different characterizations.

In order to evaluate the grain orientation induced by the different hot-pressing conditions, out-of-plane XRD patterns were performed on the samples' surface between 5 and 45° in a theta-theta PaNalyticalX'Pert Pro diffractometer (CuKα radiation, λ = 1.54059 Å). Moreover, grain orientation has been determined using Lotgering factor [30].

Microstructural and morphological characterization has been made, on the surfaces of samples after chemical etching with HCl 6 N solution in water for 5 s to reveal grain boundaries, in a field emission scanning electron microscope (FESEM, Carl Zeiss Merlin). Additionally, fractographical characterization of samples has been carried out on longitudinally fractured surfaces of samples.

The density of samples was determined through the well-known Archimedes' method, using 4.677 g/cm^3 as the theoretical density value for $Ca_3Co_4O_9$ [31]. At least 5 samples for each condition were evaluated in order to minimize measurement errors.

Simultaneous measurement of electrical resistivity and Seebeck coefficient has been made along the direction perpendicular to the applied pressure, in steady-state mode by the standard DC four-point-probe technique in a LSR-3 system (Linseis GmbH), under He atmosphere, and temperatures between 50 and 800 °C. Moreover, these data were used to determine the electrical performances through the power factor, PF, which is defined as $PF = S^2/\rho$. The thermal diffusivity (α) has been determined in all samples, perpendicularly to the applied pressure, in a laser-flash system (Linseis LFA 1000). The thermal conductivity (κ) was obtained using the formula:

$$\kappa = \alpha\, C_p \rho \qquad \text{Eq. 2}$$

where C_p is the specific heat, calculated through the well-known Dulong-Petit law, and ρ is the sample density previously determined. Using the power factor, and κ, the thermoelectric performances of samples (ZT) have been calculated. Dilatometric characterization has been performed, in the direction perpendicular to the external pressure, between room temperature and 800 °C in an L79 HCS device (Linseis GmbH) in order to determine the linear expansion coefficient of all samples.

Finally, the mechanical characterization of samples was made, on surfaces perpendicular to the applied pressure direction, through Vickers microhardness, and flexural strength. Vickers microhardness has been measured in a Vickers indentation system (Matsuzawa MXT70) in several samples with 2.94 N applied load, and 15s dwell time following the procedure commonly described [32]. Vickers hardness has been calculated using the formula:

$$HV = 1.8544\frac{F}{d^2} \qquad \text{Eq. 3}$$

where HV is microhardness in MPa, F is the applied load in N, and d is the vertical and horizontal diagonals mean value of each indentation, in mm. The flexural strength has been obtained through three points bending tests in an Instron 5565 machine with a 10 mm loading span fixture and a punch displacement speed of 30 μm/min, as described elsewhere [33].

3. Results and discussion

3.1. Structural characterization

The out-of-plane XRD patterns of $Ca_{0.93}Sr_{0.07}Co_4O_9$ samples hot-pressed under different conditions are shown in Fig. 1and A1, between 5 and 45°, for clarity. As it can be observed in these graphs, all samples display very similar diffraction patterns and all peaks are associated to the 349 phase with monoclinic symmetry [30], in agreement with the PDF cards #00-058-0661 & #00-023-0110, and with previously published data [34,35]. These data clearly point out to the absence of secondary phases after the hot pressing procedure. Moreover, the highest peaks in the graphs correspond to the (*00l*) diffraction planes (indexed in the plots), which indicates a strong grain orientation with their *ab*-planes preferentially aligned along the perpendicular direction with respect to the applied pressure during the hot pressing process. In order

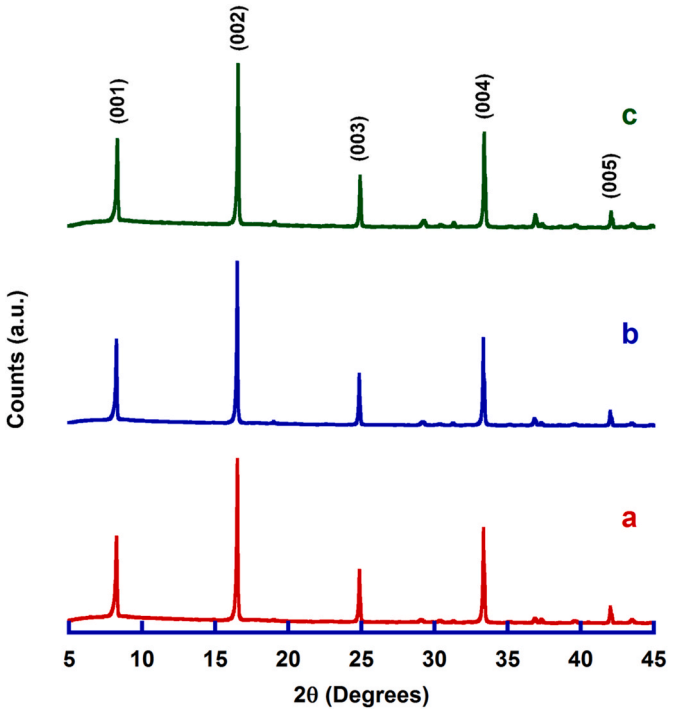

Fig. 1. Out-of-plane XRD graph for samples prepared through hot-pressing process at 800 °C under different applied pressures, a) 51; b) 61; and c) 71 MPa. Indexed peaks indicate the (*00l*) reflections of $Ca_{2.93}Sr_{0.07}Co_4O_9$ phase.

Table 1
Calculated Lotgering factor of all samples, as a function of temperature and applied pressure, after the hot-pressing process.

	800 °C	850 °C	900 °C
51 MParowhead	0.86	0.90	0.91
61 MParowhead	0.88	0.91	0.94
71 MParowhead	0.89	0.93	0.95

to evaluate the evolution of grain orientation as a function of the hot-pressing conditions, Lotgering factor has been calculated for all samples and the results are displayed in Table 1. These data clearly show that grain alignment is increased when the applied pressure is raised, independently of the processing temperature. Moreover, the use of higher temperatures also improves grain orientation, which is more important from 800 to 850 °C than from 850 to 900 °C. The fact that higher pressures or temperatures increases grain orientation is easily understandable; however, the lower increase at 900 °C can be explained by higher grains connectivity produced at this temperature, which can limit the grain movement toward the preferred orientation.

FESEM observations on the samples surfaces have shown that grain sizes are increased when the hot-pressing temperature is raised, as illustrated in Fig. A2. Moreover, besides this effect, porosity is also reduced when the external applied pressure is increased, as illustrated in Fig. A3. These microstructural modifications are clearly reflected in Fig. 2, where the lowest and highest temperature and pressure conditions are shown on the chemical etched surfaces of samples. From these images, it is clear that the largest grain sizes and the lowest porosity content is obtained in hot-pressed samples at 900 °C under an external applied pressure of 71 MPa.

This evolution has been confirmed through density measurements

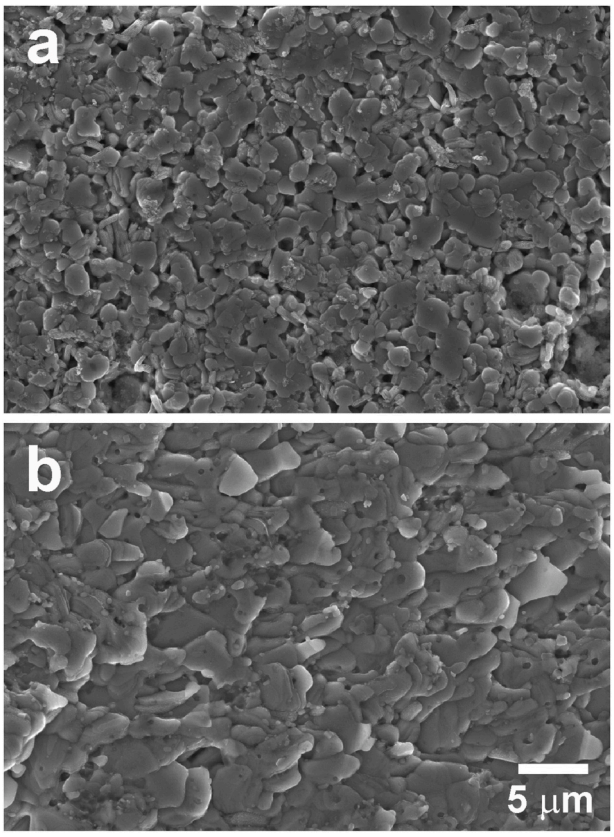

Fig. 2. Representative FESEM micrographs of samples surfaces, after chemical etching, for samples produced using the lowest and highest T, and P conditions for the hot-pressing process. a) 800 °C and 51 MPa; and b) 900 °C and 71 MPa.

Table 2
Density and Standard error for all samples, in g/cm^3, as a function of temperature and applied pressure, after the hot-pressing process.

	800 °C	850 °C	900 °C
51 MParowhead	4.17 ± 0.09	4.17 ± 0.04	4.19 ± 0.08
61 MParowhead	4.21 ± 0.05	4.27 ± 0.05	4.30 ± 0.08
71 MParowhead	4.27 ± 0.06	4.29 ± 0.04	4.45 ± 0.07

using Archimedes' method, as it is presented in Table 2. Even if no drastic modifications are produced in these samples, some trends can be extracted from these data. Higher temperatures or pressures during the hot-pressing process lead to higher density values. Moreover, the lowest values are obtained in samples processed at 800 °C and 51 MPa (4.17 g/cm^3, 89% of the theoretical one), while the highest ones have been determined in those prepared at 900 °C and 71 MPa (4.45 g/cm^3, 95% of the theoretical one). These values are very similar to those reported for highly densified materials, around 95–98% of the theoretical density [21,26] and much higher than the obtained in pressureless sintered materials, 60–79% [21,27].

3.2. . *Microstructural and mechanical characterization*

When observing fractured surfaces of the samples, it has been found that grain alignment shows the same trends observed in grain sizes evolution already discussed in Fig. 2, it is enhanced when temperature or pressure is increased, as displayed in Fig. 3. Fig. A4 is illustrating the

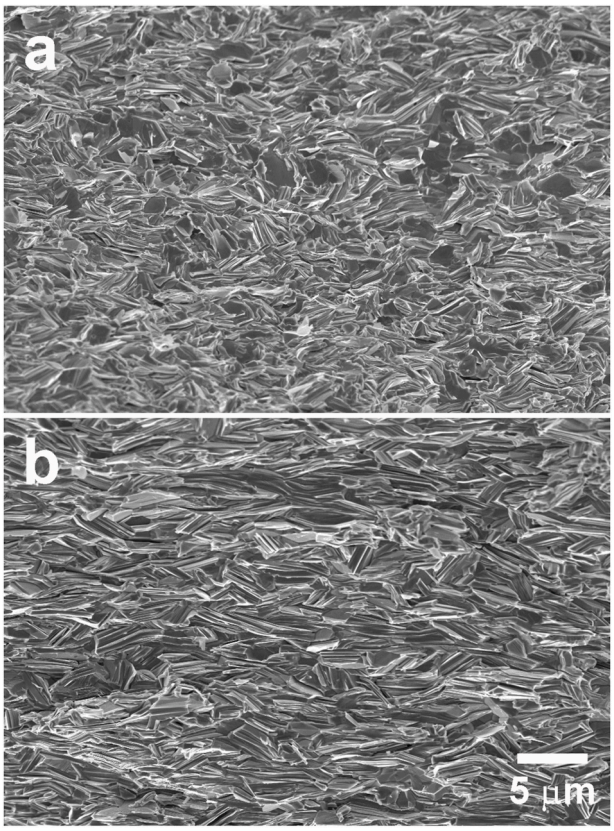

Fig. 3. Representative FESEM micrographs of fractured surfaces for samples produced using the lowest and highest T, and P conditions for the hot-pressing process. a) 800 °C and 51 MPa; and b) 900 °C and 71 MPa.

evolution of grain alignment with hot-pressing temperature when the pressure is maintained constant. As it can be observed in the micrographs, higher temperature leads to larger and better-oriented grains, with their ab-planes preferentially oriented perpendicularly to the applied pressure direction. Moreover, when the pressure is increased at a constant hot-pressing temperature, grain sizes and orientation are also enhanced, but in much lower extent than the produced by temperature, as seen in Fig. A5.

The microstructural modifications previously observed are reflected in the macroscopic properties of $Ca_{2.93}Sr_{0.07}Co_4O_9$ samples, as it can be observed in Fig. 4, where flexural strength is presented as a function of applied temperatures and pressures during the hot-pressing process. As it can be easily seen, mechanical properties are increased when temperature and/or pressure is increased, reaching the highest values for hot-pressed samples at 900 °C and 71 MPa (247 MPa), which is much higher than the obtained in pristine sintered materials, between 18 and 56 MPa [36–38]. Moreover, they are around two times higher than the obtained in B_4C or Ag added sintered materials, 126 and 118 MPa, respectively [37,38]. Moreover, they are in the range of hot-pressed materials for 24 h, 254 MPa [36], and lower than the obtained in hot-pressed $Ca_{2.93}Sr_{0.07}Co_4O_9$ samples for more than 12 h (295 MPa) [39], or in SPS materials (284 MPa) [36].

The Vickers microhardness evolution with the processing conditions is shown in Fig. 5. As it can be easily observed in the graph, it follows the same trends observed in the flexural strength measurements previously discussed, reflecting the effect of grain growth and orientation on these mechanical properties. The highest values (around HV 250 MPa) have been determined in $Ca_{2.93}Sr_{0.07}Co_4O_9$ samples hot pressed at 900 °C under 71 MPa applied pressure. This is higher than the highest values reported by using nanoindentation through hot pressing (HV 230 MPa) [36], which should not be influenced by the effect of grain boundaries. On the other hand, it is lower than the reported for SPS processed materials at 75 MPa, using nanohardness (HV 310 MPa) [36].

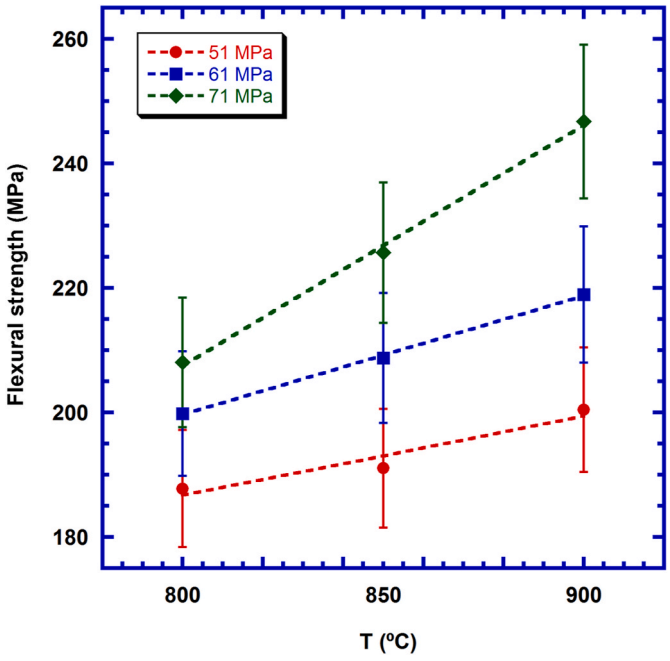

Fig. 4. The flexural strength evolution of $Ca_{2.93}Sr_{0.07}Co_4O_9$ samples, with their standard error, as a function of applied temperature and pressure in the hot-pressing process.

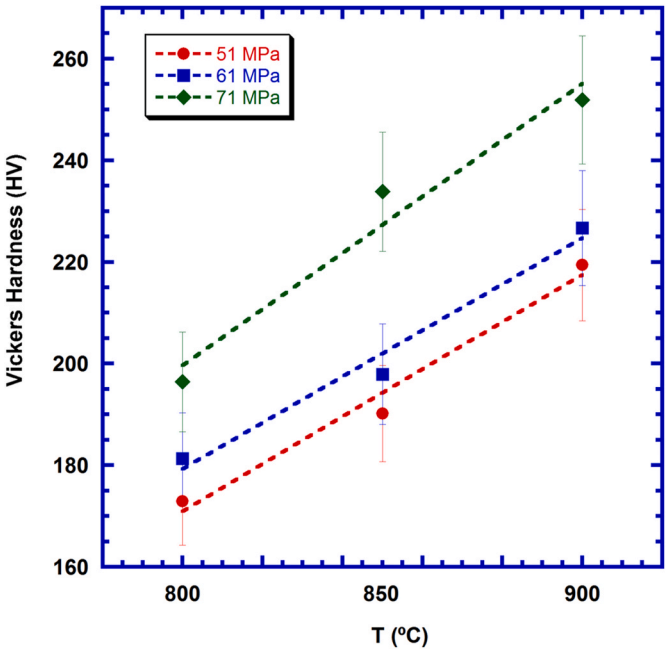

Fig. 5. Vickers hardness evolution of $Ca_{2.93}Sr_{0.07}Co_4O_9$ samples, with their standard error, as a function of applied temperature and pressure in the hot-pressing process.

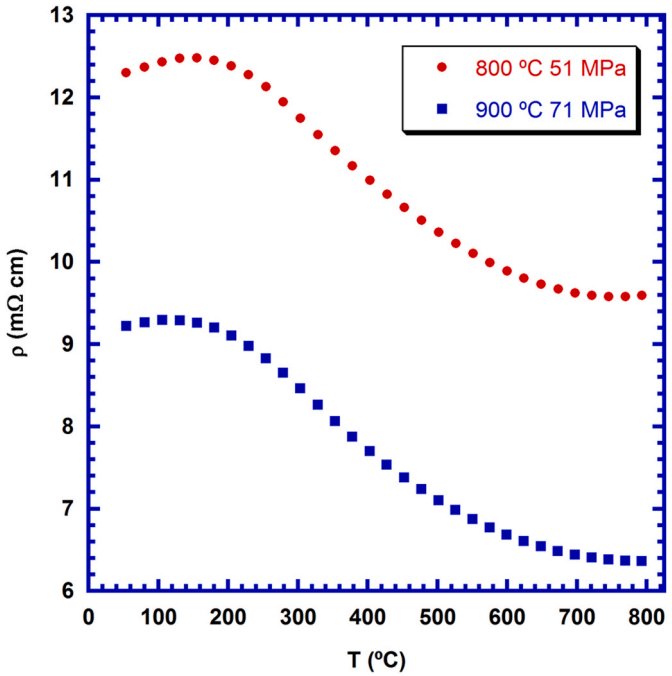

Fig. 6. Electrical resistivity evolution, as a function of temperature, for samples produced using the lowest and highest T, and P conditions for the hot-pressing process.

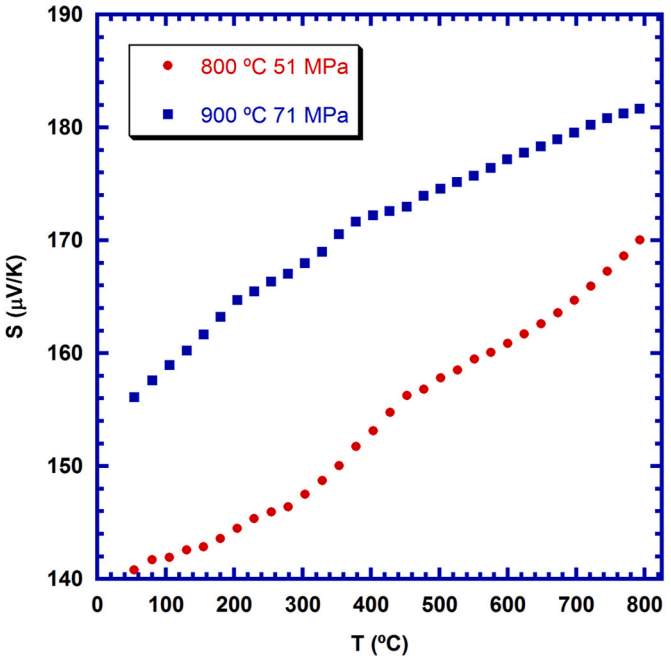

Fig. 7. Seebeck coefficient evolution, as a function of temperature, for samples produced using the lowest and highest T, and P conditions for the hot-pressing process.

3.3. Electrical characterization

The temperature dependence of the electrical resistivity, for the $Ca_{2.93}Sr_{0.07}Co_4O_9$ samples hot-pressed at the lowest and highest T and P conditions, is shown in Fig. 6. As it can be seen in this graph, a reduction of around 10% is produced at the highest conditions, when compared to the lowest ones. This is due to the decrease of the resistivity induced by the raise of temperatures, as it is shown in Fig. A6. However, by inspecting Fig. A7 an effect related to the pressure also must be participating in this reduction. Moreover, this evolution is in agreement with the microstructural evolution previously discussed, probably due to an enhancement on the charge carrier mobility, which has been confirmed by using the Weighted Mobility (μ_w) introduced by Snyder et al. [40]. This evolution can be illustrated by the values determined for the samples prepared at 900 °C and 51, 61, and 71 MPa: 29.8, 27.3, and 23.0 $cm^2/(V\,s)$, respectively, while for samples prepared at 800 °C and 61 MPa was 18.8 $cm^2/(V\,s)$. These values are in the range, but slightly higher, than those previously reported in the literature [41], explaining the lower electrical resistivity of the samples prepared in this work. Otherwise, all samples display the same behavior with respect to temperature; they have a slight metallic-like behavior from room temperature to about 150 °C, changing to semiconducting-like at higher temperatures. This change can be associated to a modification of the transport mechanism, as previously reported; in the metallic regime charge carriers are moving along the conduction or valence bands [42,43], while in the semiconducting it is a thermally activated hole-hopping along the conduction layer from Co^{4+} to Co^{3+} [44,45]. This transition temperature only slightly changes with the hot pressing conditions. As a consequence of this semiconducting behavior at high temperatures, all samples reach their minimum resistivity values at 800 °C. Moreover, the lowest electrical resistivity within the different samples has been obtained in hot-pressed samples at 900 °C and 71 MPa (6.4 mΩ cm). This minimum resistivity is around the best reported for materials prepared by classical SPS (6.0–9.0 mΩ cm) [26,46,47], or edge-free SPS (about 7.0 mΩ cm) [21]. On the other hand, it is much lower than the typically reported for hot-pressed materials (25 mΩ cm) [20], or in sintered materials with the same substitutions (15 mΩ cm)

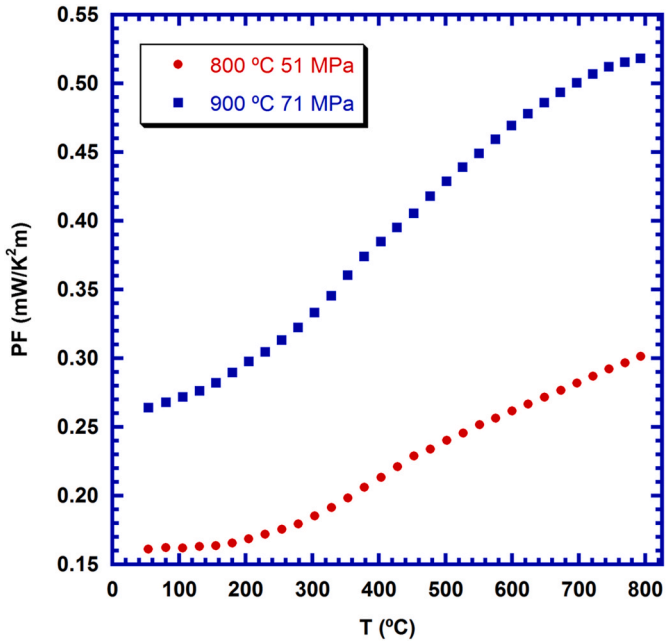

Fig. 8. Power factor evolution, as a function of temperature, for samples produced using the lowest and highest T, and P conditions for the hot-pressing process.

[27]. These data clearly reflect the good grain orientation and the high density obtained in these materials previously discussed.

The temperature dependence of the Seebeck coefficient, for the $Ca_{2.93}Sr_{0.07}Co_4O_9$ samples hot-pressed at the lowest and highest T and P conditions, is shown in Fig. 7. As it can be observed in the graph, S is positive in the whole measured temperature range, which is associated to a hole predominant charge carrier transport. Moreover, it is increased linearly with temperature in all cases, which is the typical behavior of metals or degenerated semiconductors when the variation of different parameters with temperature, as carrier concentration, effective mass, and Fermi level, are negligible [48]. The evolution of Seebeck coefficient values as a function of temperature or pressure during the hot pressing process is illustrated in Figures A8 and A9, respectively, where it can be seen that S is increased with processing temperatures and pressures. This evolution can be associated to a decrease of charge carrier concentration, in agreement with Koshibae's equation [49], when the hot pressing temperatures or pressures are increased. Consequently, the highest S values have been determined at 800 °C in samples processed at 900 °C under 71 MPa applied pressure (182 μV/K). These values are higher than the reported for pristine samples prepared through SPS (165 μV/K) [46,47], and the same obtained in SPS sintered Sr-doped samples (182 μV/K) [26]. On the other hand, it is much lower than the measured in sintered Sr-doped materials (220 μV/K) [27], due to their higher electrical resistivity.

Electrical performances of samples were determined using the electrical resistivity and Seebeck coefficient data through the power factor. In Fig. 8the evolution of PF with temperature for the samples hot-pressed at the lowest and highest T and P conditions. As it can be easily observed in the plot, the samples prepared under the highest T, and P conditions display between 60 and 70% higher PF than the obtained in the lowest conditions. This difference is due to the lower electrical resistivity and higher Seebeck coefficient values obtained in the former samples. When considering the effect of temperature at constant pressures (61 MPa), it is clear that higher temperatures lead to higher PF values in the whole measured temperature range (see Fig. A10). Moreover, the evolution of PF at constant temperature (900 °C) also indicates that higher external applied pressures induce higher PF values in the samples (see Fig. A11). The highest PF values have been obtained at 800 °C in samples hot-pressed at 900 °C under 71 MPa applied pressure (0.52mW/K^{2}m). These values are in the order of those reported in pristine samples prepared through SPS (0.50mW/K^{2}m) [46], and higher than the obtained in Sr-doped samples classically sintered, or by SPS (0.32mW/K^{2}m) [26,27].

3.4. Thermal characterization

As it is well known, total thermal conductivity is the sum of two different contributions, expressed as: $\kappa = \kappa_{ph} + \kappa_e$, where κ_{ph} is the phonon contribution (or lattice thermal conductivity), and κ_e is the charge carrier contribution. The values of κ_e can be calculated using the Wiedermann-Franz's law [50], which relates thermal electronic and electrical conductivity through the expression:

$$\kappa_e = L\,\sigma\,T \qquad \text{Eq. 4}$$

where L is the Lorentz number (2.45×10^{-8} V^2/K^2), σ the electrical conductivity, and T the absolute temperature.

In Fig. 9, the variation of κ_{ph}, and κ_e with temperature for the samples hot-pressed at the highest and lowest T, and P, is presented. As it can be seen in this graph, electronic thermal conductivity is increased with temperature, which is in agreement with the decrease of electrical resistivity previously discussed. On the other hand, total thermal conductivity tends to decrease when the temperature is raised up to around 600 °C, in all cases. This decrease is due to the enhancement of phonon scattering induced by the increase of lattice vibrations. Moreover, at higher temperatures, the total thermal conductivity rises as a consequence of the higher contribution of the electronic one. When considering the effect of processing temperatures and pressures, a no clear trend can be observed in the total thermal conductivity as it is illustrated in Fig. A12 and A13; this is probably due to internal stresses which can help to scatter phonons in some of the samples. The minimum κ determined in these samples at 800 °C (~1.51 W/(K*m)) has been found in the ones processed at 800 °C and 51 MPa. These values are very close to the measured in samples processed at 900 °C and 61 MPa (around 1.53 W/(K*m)). Furthermore, they are much higher than the reported in low

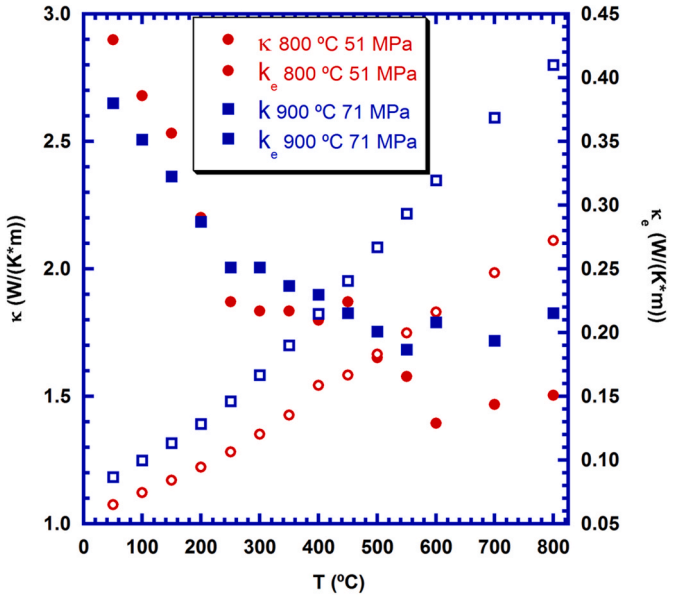

Fig. 9. Total and electronic thermal conductivity, as a function of temperature, for samples produced using the lowest and highest T, and P conditions for the hot-pressing process.

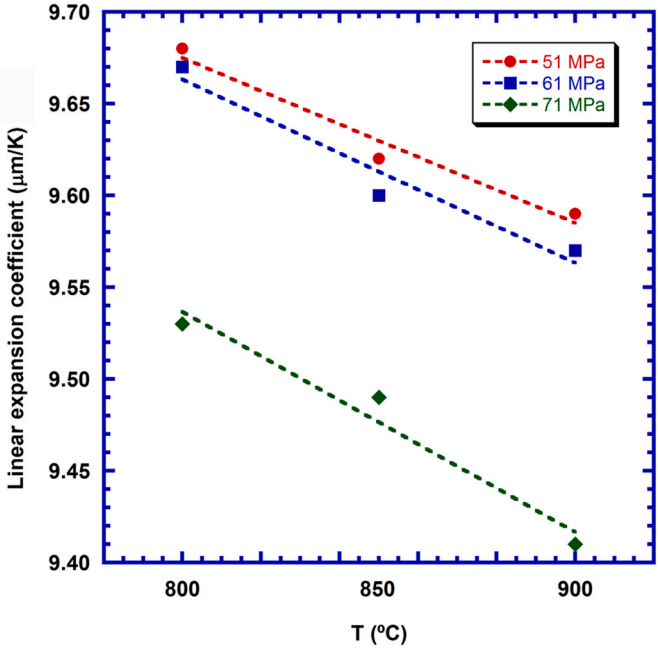

Fig. 10. Thermal expansion coefficient of samples, measured between room temperature and 800 °C, as a function of P, and T in the hot-pressing process. The dashed lines are guides for the eyes.

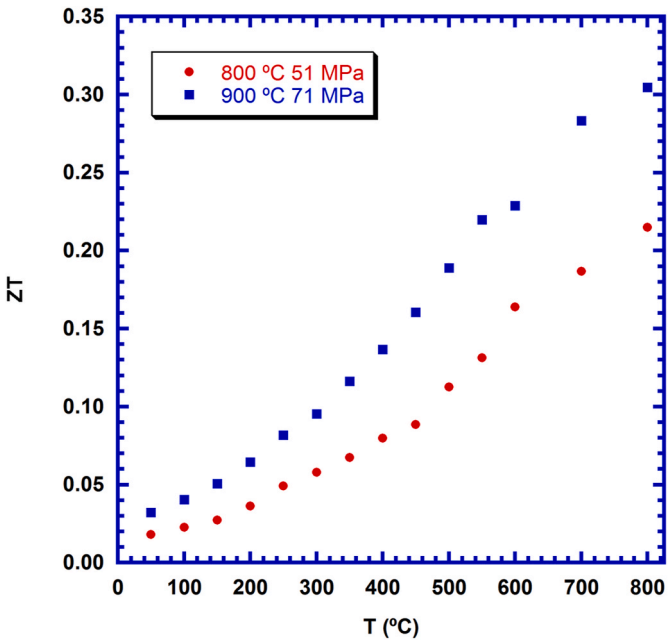

Fig. 11. ZT evolution, as a function of temperature, for samples produced using the lowest and highest T, and P conditions for the hot-pressing process.

density (about 60% theoretical density) samples, with randomly oriented grains, prepared through the classical solid-state method (0.9 W/(K*m)) [51]. Contrarily, these values are much lower than the obtained, at the same temperature, in high density undoped materials prepared using SPS (2.1 W/(K*m)) [52], or in high density textured samples processed through hot-uniaxial pressing (between 2.2 and 3 W/(K*m)) [20,51].

The microstructural modifications induced by the different conditions used in the hot pressing process also influence the thermal expansion coefficient, as shown in Fig. 10, where it is presented as a function of the hot pressing conditions. The dashed lines are only guides for the eyes to follow the evolution with temperature at a constant pressure. As it can be easily seen in the plot, thermal expansion coefficient decreases nearly linearly with the processing temperature, while this decrease is much more evident with pressure, especially for the samples processed with 71 MPa external pressure. The minimum value determined in this work is around 9.41 ppm/K for the samples processed at the highest T, and P. This value is lower than the reported in $Ca_3Co_4O_9$ samples (12.8 ppm/K) [53], or in Ca-substituted materials (10.6–12.9 ppm/K) [53,54]. Even if this reduction seems to be minor, it should be highlighted that it is closer to that of the alumina (7.5 ppm/K) [55], which is used as structural ceramic in the thermoelectric modules architecture. Consequently, the thermal stresses appearing in the hot side of these modules, due to the different thermal expansion of components, is reduced, leading to the enhancement of their lifespan.

3.5. . *Thermoelectric performances*

The thermoelectric performances of all samples have been evaluated through the ZT values, calculated using Eq. (1). It has been found that ZT values are higher when the temperature and pressure of hot-pressing process are increased, as shown in Fig. 11. When considering the individual effect of T, and P, the evolution of ZT can be explained as follows: when the hot-pressing temperature is raised, ZT values are larger, as illustrated in Fig. A14; on the other hand, even if the effect of pressure is exactly the same for the samples prepared at 800 °C, at higher temperatures, the highest ZT values are obtained for the materials prepared under 61 MPa, as illustrated in Fig. A15. Consequently, the highest ZT values at 800 °C (~0.35) have been determined in samples processed at 900 °C and 61 MPa. These values are much higher than the typical obtained in pristine sintered materials (0.08) [51], SPS processed (0.06–0.30) [56–59], or hot pressed samples (0.005–0.18) [20,51,60]. Moreover, it is higher than the reported for Sr-doped materials prepared by SPS (0.22) [26].

All these data clearly show that the materials prepared in this work possess the best thermoelectric performances reported in the literature for bulk specimens, to the best of our knowledge.

4. . Conclusions

In this study, Sr-doped $Ca_3Co_4O_9$ materials have been successfully prepared through hot-pressing process under different temperatures and pressures (between 800 and 900 °C, and 51–71 MPa, respectively). XRD data have demonstrated that all samples are composed by the thermoelectric phase. Grain alignment has been shown to be influenced by temperature and pressure. Moreover, grain sizes increase with T, and P, while porosity is decreased. All samples have excellent mechanical performances, 247 MPa flexural strength, and 250 MPa Vickers microhardness, which are similar or higher than the best reported values in the literature for samples prepared under equivalent conditions. The minimum values determined at 800 °C through electrical resistivity measurements (6.4 mΩ cm in samples processed at 900 °C and 71 MPa) are within the lowest ones in the literature. The highest S values have also been determined in these samples, 182 μV/K, similar to the best values found in highly dense textured materials. On the other hand, the lowest κ values have been measured in samples processed at 800 °C and 51 MPa, or 900 °C and 61 MPa (1.51, and 1.53 W/K m, respectively). Finally, the highest ZT value has been obtained for samples processed at 900 °C and 61 MPa (0.35), which is higher than the best reported in the literature for bulk textured materials, to the best of our knowledge. Furthermore, it should be highlighted that these materials have been prepared after a total thermal treatment of just 2 h.

Declaration of competing interest

The authors declare that they have no known competing financial interests or personal relationships that could have appeared to influence the work reported in this paper.

Acknowledgements

The authors wish to thank the Spanish MINECO-FEDER project (MAT2017-82183-C3-1-R) and the Aragón Government (Research Group T54-20R), for their <grant-highlight>financial support</grant-highlight>. The Regional Development Agency of the Basque Country (SPRI) is acknowledged for the economic <grant-highlight>support</grant-highlight> through the Programa ELKARTEK (KK-2020/00113, HARVESTGEN research project). The use of Servicio General de Apoyo a la Investigación-SAI, Universidad de Zaragoza is also acknowledged.

Annex.

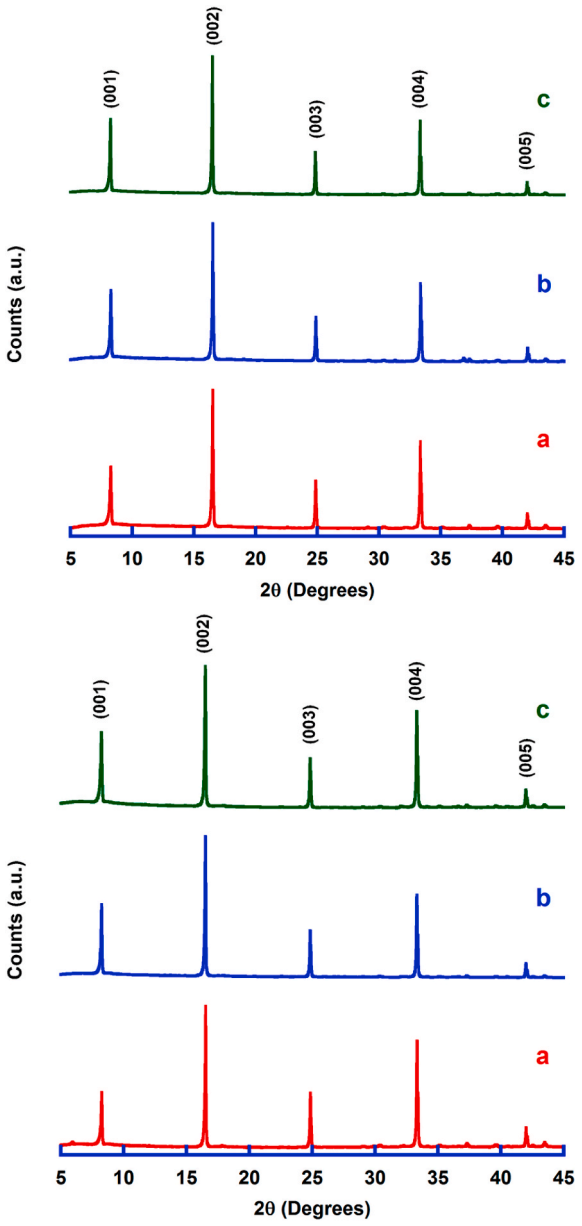

Fig. A1. Out-of-plane XRD graph for samples prepared through hot-pressing process at 850 (upper graph) and 900 °C (lower graph), under different applied pressures, a) 51; b) 61; and c) 71 MPa. Indexed peaks indicate the (*00l*) reflections of $Ca_{2.93}Sr_{0.07}Co_4O_9$ phase.

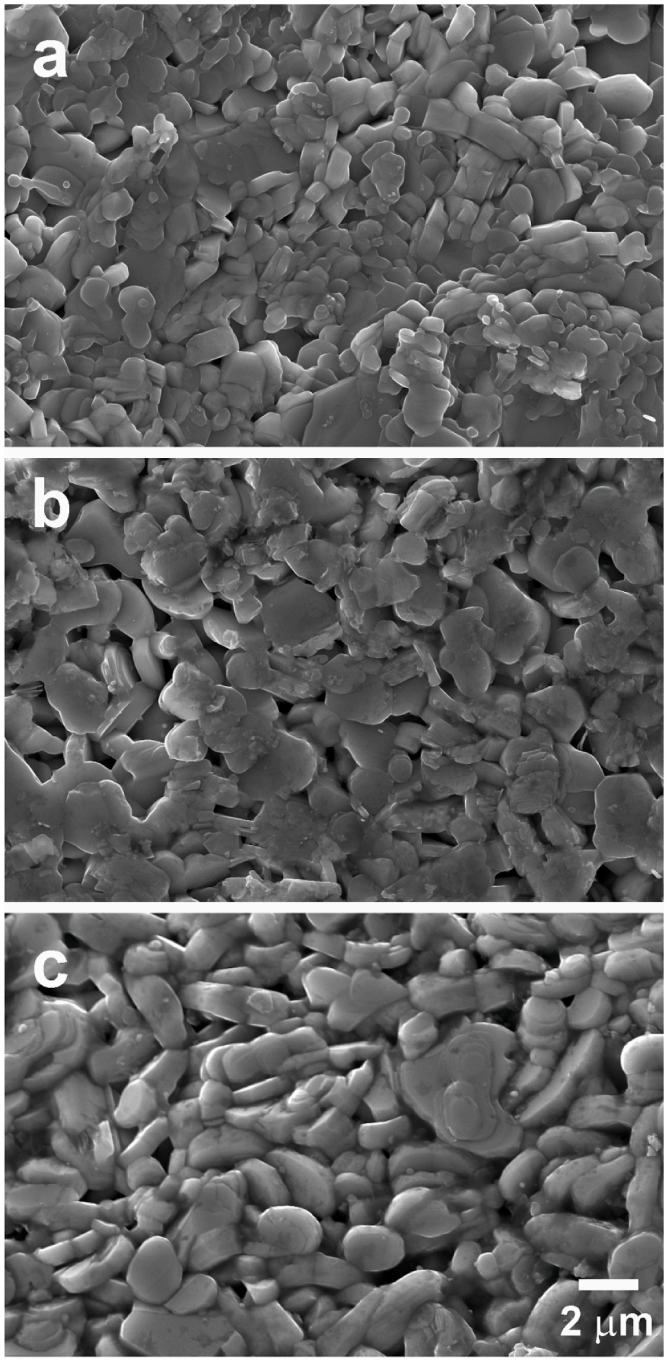

Fig. A2. Representative FESEM micrographs performed on the surfaces of hot-pressed samples at 51 MPa and different temperatures, a) 800; b) 850; and c) 900 °C.

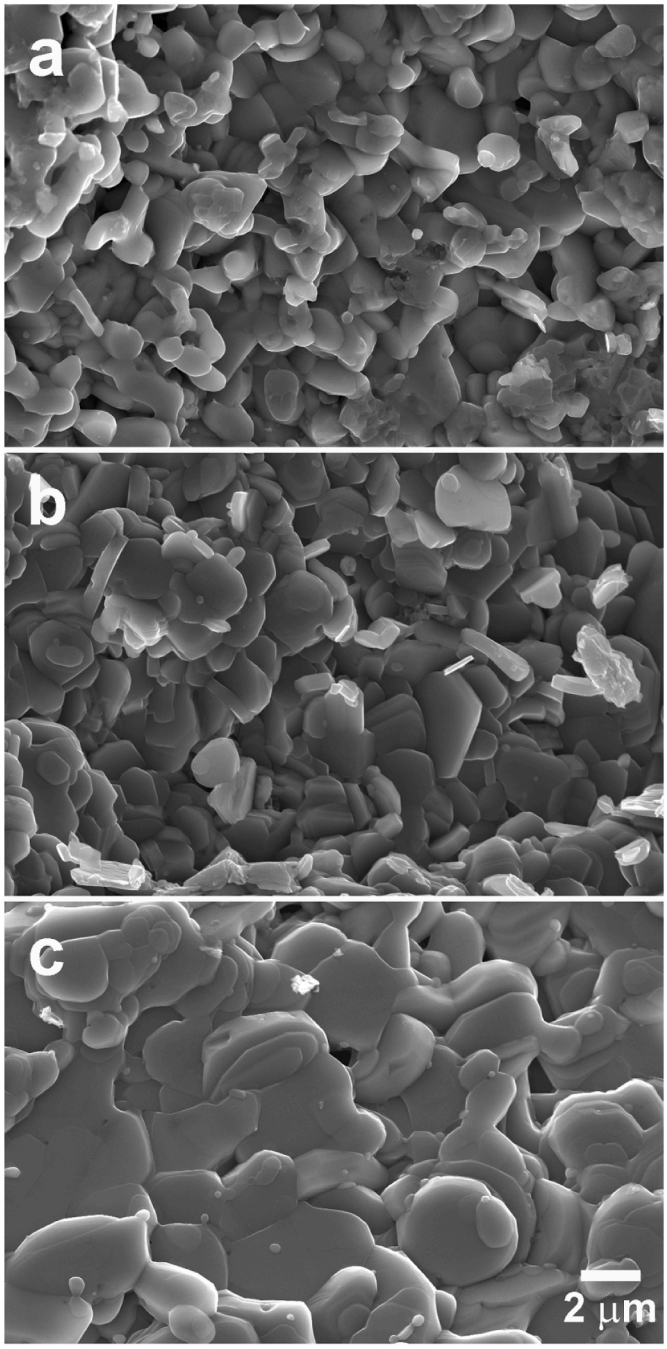

Fig. A3. Representative FESEM micrographs performed on the surfaces of hot-pressed samples at 850 °C and different applied pressures, a) 51; b) 61; and c) 71 MPa.

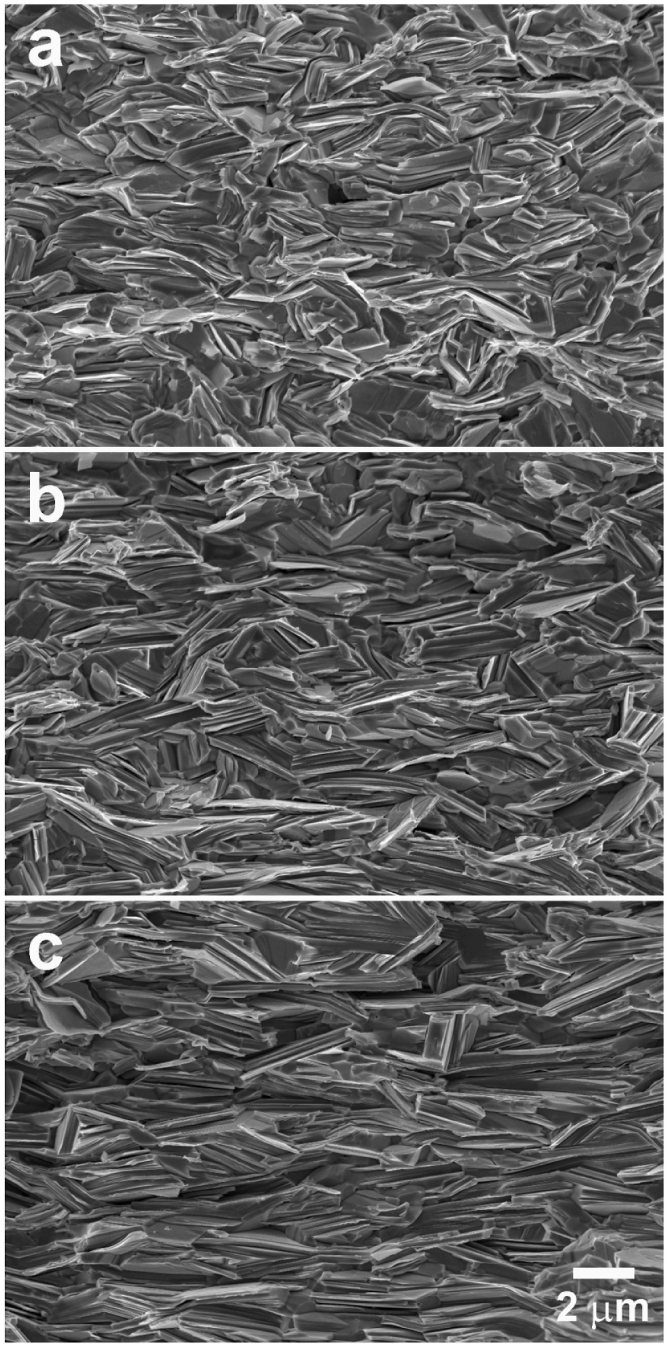

Fig. A4. Representative FESEM micrographs performed on the fractured surfaces of hot-pressed samples at 71 MPa and different temperatures, a) 800; b) 850; and c) 900 °C.

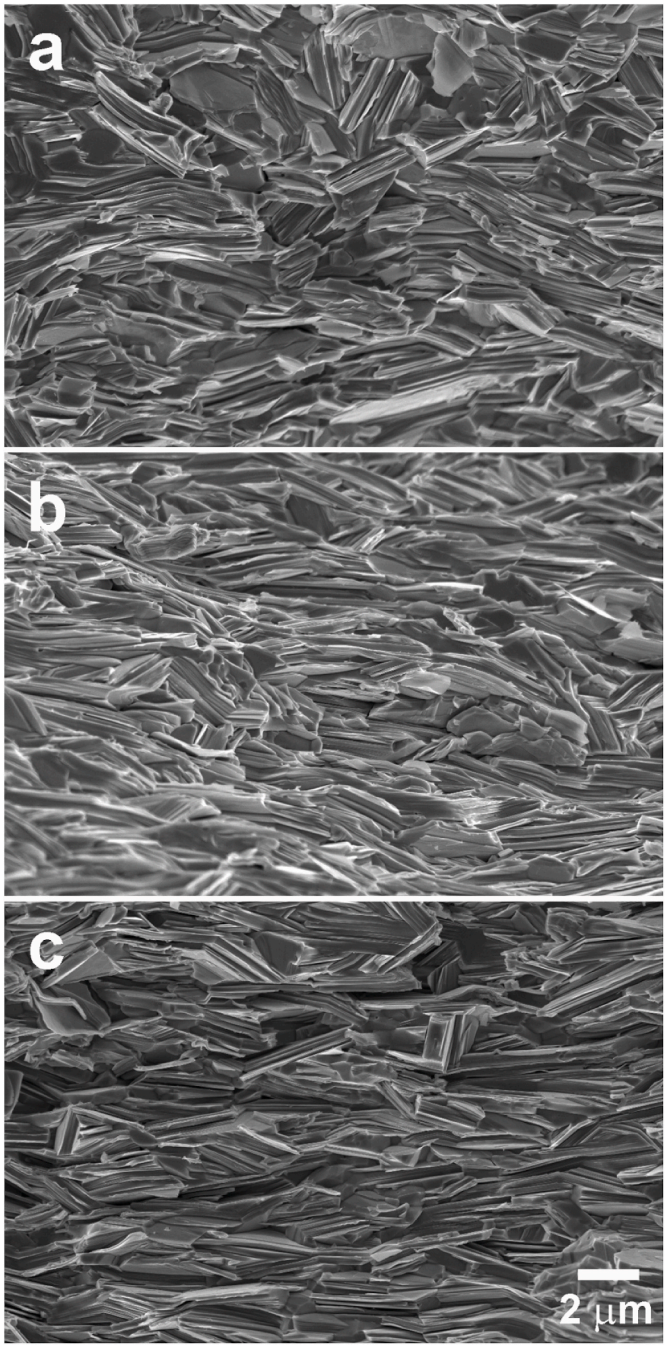

Fig. A5. Representative FESEM micrographs performed on the fractured surfaces of hot-pressed samples at 900 °C and different applied pressures, a) 51; b) 61; and c) 71 MPa.

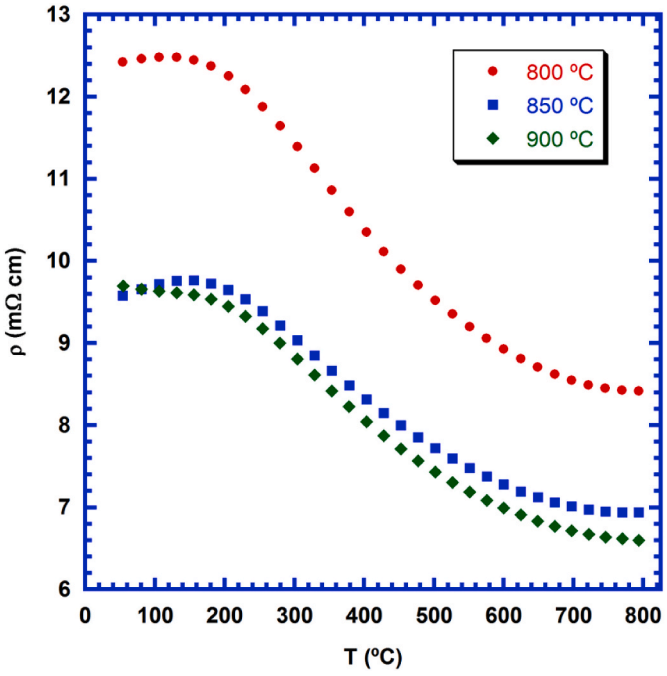

Fig. A6. Evolution of electrical resistivity in hot-pressed samples at 61 MPa and different temperatures.

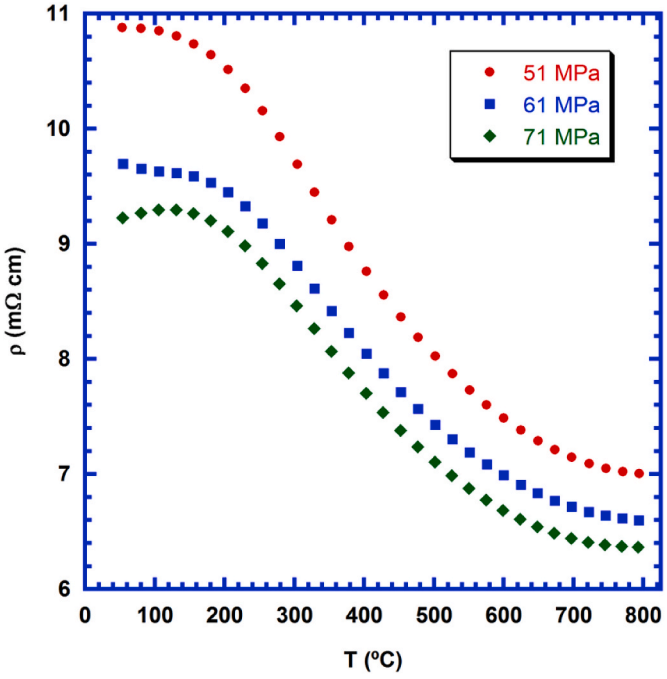

Fig. A7. Evolution of electrical resistivity in hot-pressed samples at 900 °C and different applied pressures.

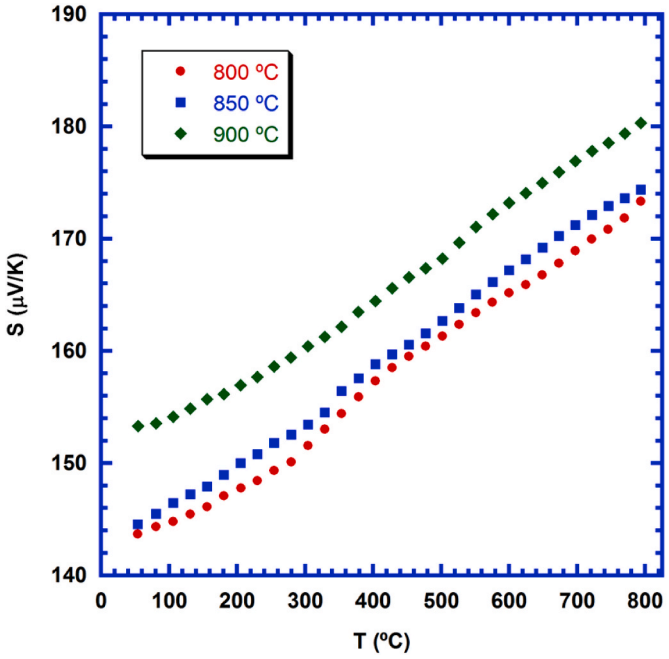

Fig. A8. Evolution of Seebeck coefficient in hot-pressed samples at 61 MPa and different temperatures.

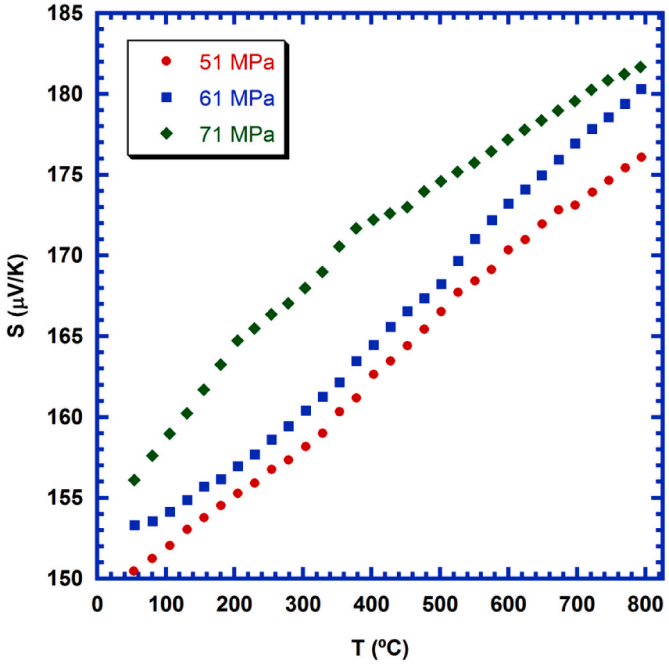

Fig. A9. Evolution of Seebeck coefficient in hot-pressed samples at 900 °C and different applied pressures.

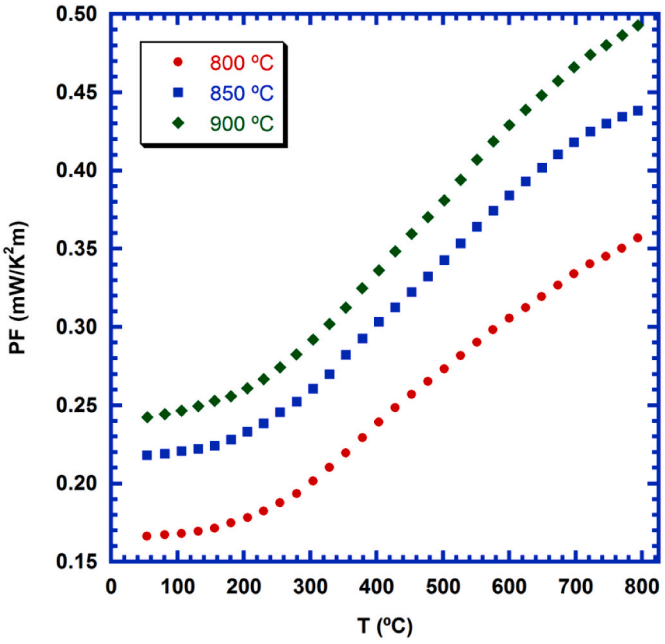

Fig. A10. Evolution of power factor with temperature determined in hot-pressed samples at 61 MPa and different temperatures.

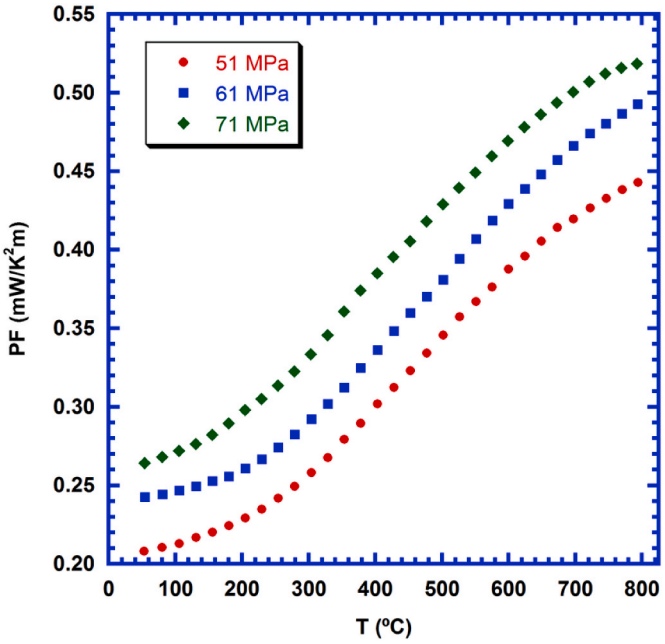

Fig. A11. Evolution of power factor with temperature determined in hot-pressed samples at 900 °C and different applied pressures.

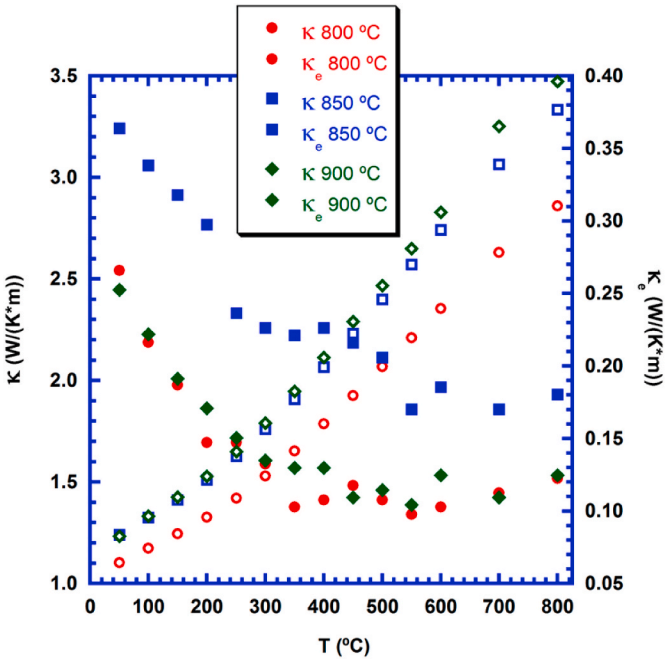

Fig. A12. Evolution of total and electronic thermal conductivity determined in hot-pressed samples at 61 MPa and different temperatures.

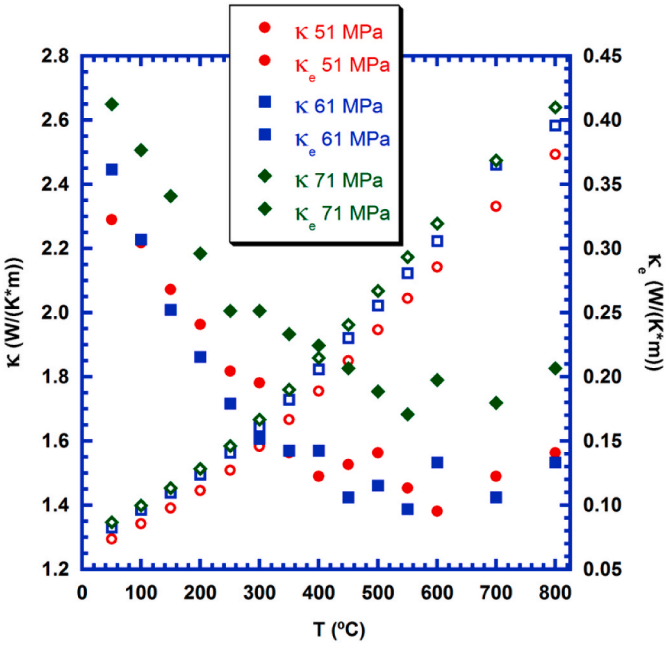

Fig. A13. Evolution of total and electronic thermal conductivity determined in hot-pressed samples at 900 °C and different applied pressures.

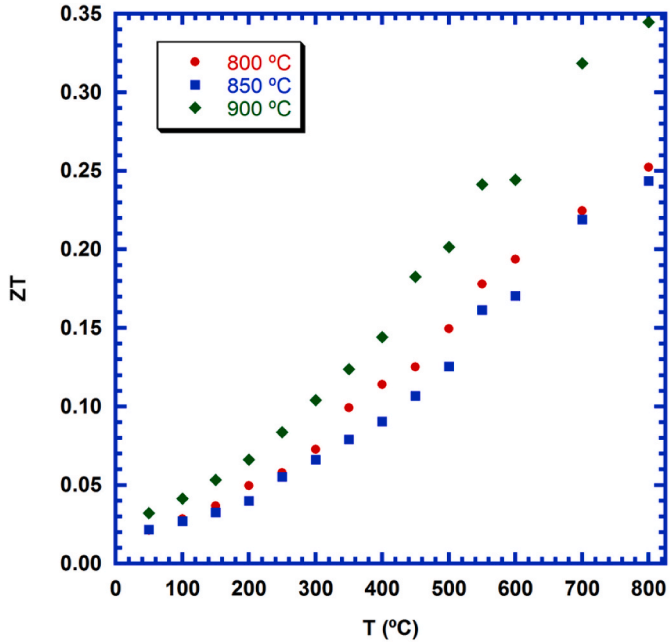

Fig. A14. Evolution of ZT values determined in hot-pressed samples at 61 MPa and different temperatures.

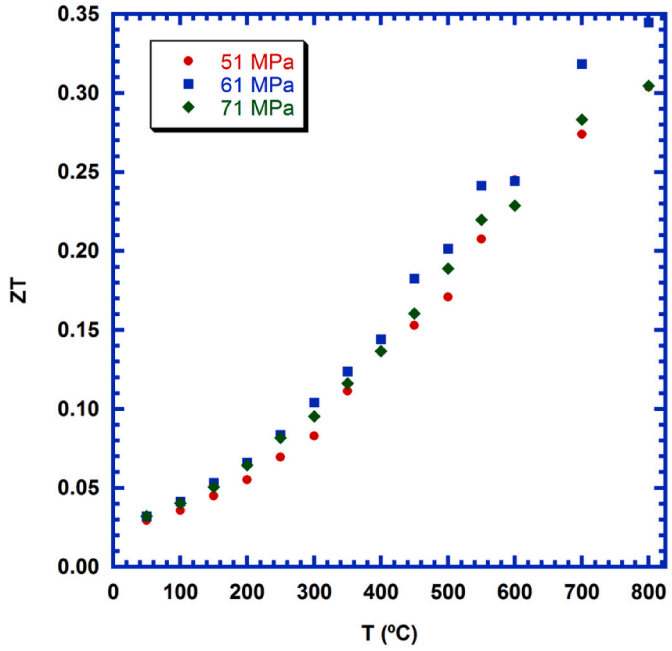

Fig. A15. Evolution of ZT values determined in hot-pressed samples at 900 °C and different applied pressures.

References

[1] R. Freer, A.V. Powell, Realising the potential of thermoelectric technology: a Roadmap, J. Mater. Chem. C 8 (2020) 441–463.
[2] A. Bahrami, G. Schierning, K. Nielsch, Waste recycling in thermoelectric materials, Adv. Energy Mater. 10 (2020) 1904159 (Pubmed Partial Author articletitle stitle stitle Volume Page).
[3] D. Beretta, N. Neophytou, J.M. Hodges, M.G. Kanatzidis, D. Narducci, M. Martin-Gonzalez, M. Beekman, B. Balke, G. Cerretti, W. Tremel, A. Zevalkink, A. I. Hofmann, C. Muller, B. Dorling, M. Campoy-Quiles, M. Caironi, Thermoelectrics: from history, a window to the future, Mater. Sci. Eng. R 138 (2019) 100501.
[4] G. Mahan, B. Sales, J. Sharp, Thermoelectric materials: new approaches to an old problem, Phys. Today 50 (1997) 42–47.
[5] D.M. Rowe, Applications of nuclear-powered thermoelectric generators in space, Appl. Energy 40 (1991) 241–271.
[6] H. Naito, Y. Kohsaka, D. Cooke, H. Arashi, Development of a solar receiver for a high-efficiency thermionic/thermoelectric conversion system, Sol. Energy 58 (1996) 191–195.
[7] D.M. Rowe, Thermoelectrics Handbook: Macro to Nano, first ed., CRC Press, Boca Raton, 2006 (Pubmed Partial Author stitle stitle Volume Page).
[8] H. Wang, J. Hwang, M.L. Snedaker, I.-H. Kim, C. Kang, J. Kim, G.D. Stucky, J. Bowers, W. Kim, High thermoelectric performance of a heterogeneous PbTe nanocomposite, Chem. Mater. 27 (2015) 944–949.
[9] H.C. Wang, J. Hwang, C. Zhang, T. Wang, W.B. Su, H. Kim, J. Kim, J.Z. Zhai, X. Wang, H. Park, W. Kim, C.L. Wang, Enhancement of the thermoelectric performance of bulk SnTe alloys via the synergistic effect of band structure modification and chemical bond softening, J. Mater. Chem. 5 (2017) 14165–14173.
[10] A.A. Yaroshevsky, Abundances of chemical elements in the earth's crust, Geochem. Int. 44 (2006) 48–55.

[11] I. Terasaki, Y. Sasago, K. Uchinokura, Large thermoelectric power in $NaCo_2O_4$ single crystals, Phys. Rev. B 56 (1997) R12685–R12687.
[12] S. LeBlanc, Thermoelectric generators: linking material properties and systems engineering for waste heat recovery applications, Sust. Mater. Technol. 1–2 (2014) 26–35.
[13] R. Funahashi, I. Matsubara, H. Ikuta, T. Takeuchi, U. Mizutani, S. Sodeoka, Oxide single crystal with high thermoelectric performance in air, Jpn. J. Appl. Phys. 39 (2000) L1127–L1129.
[14] A. Maignan, S. Hebert, M. Hervieu, C. Michel, D. Pelloquin, D. Khomskii, Magnetoresistance and magnetothermopower properties of Bi/Ca/Co/O and Bi (Pb)/Ca/Co/O misfit layer cobaltites, J. Phys. Condens. Matter 15 (2003) 2711–2723.
[15] G. Constantinescu, S. Rasekh, M.A. Torres, M.A. Madre, J.C. Diez, A. Sotelo, Enhancement of the high-temperature thermoelectric performance of Bi2Ba2Co2Ox ceramics, Scripta Mater. 68 (2013) 75–78.
[16] H. Leligny, D. Grebille, O. Perez, A.C. Masset, M. Hervieu, B. Raveau, A five-dimensional structural investigation of the misfit layer compound [Bi0.87SrO2]2 [CoO2]1.82, Acta Crystallogr. B 56 (2000) 173–182.
[17] A. Maignan, D. Pelloquin, S. Hebert, Y. Klein, M. Hervieu, Thermoelectric power in misfit cobaltites ceramics: optimization by chemical substitutions, Bol. Soc. Esp. Ceram. V. 45 (2006) 122–125.
[18] Sh Rasekh, F.M. Costa, N.M. Ferreira, M.A. Torres, M.A. Madre, J.C. Diez, A. Sotelo, Use of laser technology to produce high thermoelectric performances in Bi2Sr2Co1.8Ox, Mater, Design 75 (2015) 143–148 (Pubmed Partial Author articletitle stitle stitle Volume Page).
[19] K. Miyazawa, F. Amaral, A.V. Kovalevsky, M.P.F. Graca, Hybrid microwave processing of Ca3Co4O9 thermoelectrics, Ceram. Int. 42 (2016) 9482–9487.
[20] H. Wang, X. Sun, X. Yan, D. Huo, X. Li, J.-G. Li, X. Ding, Fabrication and thermoelectric properties of highly textured Ca9Co12O28 ceramic, J. Alloys Compd. 582 (2014) 294–298.
[21] J.G. Noudem, D. Kenfaui, D. Chateigner, M. Gomina, Toward the enhancement of thermoelectric properties of lamellar Ca3Co4O9 by edge-free spark plasma texturing, Scripta Mater. 66 (2012) 258–260.
[22] T. Tani, H. Itahara, H. Kadoura, R. Asahi, Crystallographic orientation analysis on calcium cobaltite ceramic grains textured by reactive-templated grain growth, Int. J. Appl. Ceram. Technol. 4 (2007) 318–325.
[23] A. Sotelo, E. Guilmeau, M.A. Madre, S. Marinel, J.C. Diez, M. Prevel, Fabrication and properties of textured Bi-based cobaltite thermoelectric rods by zone melting, J. Eur. Ceram. Soc. 27 (2007) 3697–3700.
[24] N.M. Ferreira, Sh Rasekh, F.M. Costa, M.A. Madre, A. Sotelo, J.C. Diez, M. A. Torres, New method to improve the grain alignment and performance of thermoelectric ceramics, Mater. Lett. 83 (2012) 144–147.
[25] O.-J. Kwon, W. Jo, S. Yoon, D. Shin, H. You, K. Choi, J.-S. Kim, C. Park, Relation between Seebeck coefficient and lattice parameters of (Ca2-ySryCoO3)xCoO2, J. Electron. Mater. 41 (2012) 1513–1518.
[26] F. Delorme, C.F. Martin, P. Marudhachalam, D.O. Ovono, G. Guzman, Effect of Ca substitution by Sr on the thermoelectric properties of Ca3Co4O9 ceramics, J. Alloys Compd. 509 (2011) 2311–2315.
[27] G. Constantinescu, Sh Rasekh, M.A. Torres, J.C. Diez, M.A. Madre, A. Sotelo, Effect of Sr substitution for Ca on the Ca3Co4O9 thermoelectric properties, J. Alloy, Compd 577 (2013) 511–515.
[28] H. Amaveda, M.A. Madre, M. Mora, M.A. Torres, A. Sotelo, Reduction in processing time in Ca3Co4O9+δ ceramics through nanoprecursors produced by an easily scalable and environmentally friendly process, Nanomaterials 10 (2020) 2533.
[29] M.A. Torres, G. Garcia, I. Urrutibeascoa, M.A. Madre, J.C. Diez, A. Sotelo, Fast preparation route to high-performances textured Sr-doped Ca3Co4O9 thermoelectric materials through precursor powder modification, Sci. China Mater. 62 (2019) 399–406.
[30] R. Furushima, S. Tanaka, Z. Kato, K. Uematsu, Orientation distribution–Lotgering factor relationship in a polycrystalline material—as an example of bismuth titanate prepared by a magnetic field, J. Ceram. Soc. Jpn. 118 (2010) 921–926.
[31] A.C. Masset, C. Michel, A. Maignan, M. Hervieu, O. Toulemonde, F. Studer, B. Raveau, J. Hejtmanek, Misfit-layered cobaltite with an anisotropic giant magnetoresistance: Ca3Co4O9, Phys. Rev. B 62 (2000) 166–175.
[32] B. Ozkurt, The influence of WO3 nano-particle addition on the structural and mechanical properties of Bi1.8Sr2Ca1.1Cu2.1Oy ceramics, J. Mater. Sci. Mater. Electron. 24 (2013) 4233–4239.
[33] F. Kahraman, J.C. Diez, Sh Rasekh, M.A. Madre, M.A. Torres, A. Sotelo, The effect of environmental conditions on the mechanical and thermoelectric properties of Bi2Ca2Co1.7Ox textured rods, Ceram. Int. 41 (2015) 6358–6363.
[34] E. Woermann, A. Muan, Phase equilibria in the system CaO-cobalt oxide in air, J. Inorg. Nucl. Chem. 32 (1970) 1455–1459.
[35] D. Sedmidubsky, V. Jakes, O. Jankovsky, J. Leitner, Z. Sofer, J. Hejtmanek, Phase equilibria in Ca-Co-O system, J. Solid State Chem. 194 (2012) 199–205.
[36] D. Kenfaui, M. Gomina, D. Chateigner, J.G. Noudem, Mechanical properties of Ca3Co4O9 bulk oxides intended to be used in thermoelectric generators, Ceram. Int. 40 (2014) 10237–10246.
[37] H. Amaveda, M. Mora, O.J. Dura, M.A. Torres, M.A. Madre, S. Marinel, A. Sotelo, Drastic enhancement of mechanical properties of Ca3Co4O9 by B4C addition, J. Eur. Ceram. Soc. 41 (2021) 402–408.
[38] F. Kahraman, M.A. Madre, Sh Rasekh, C. Salvador, P. Bosque, M.A. Torres, J. C. Diez, A. Sotelo, Enhancement of mechanical and thermoelectric properties of Ca3Co4O9 by Ag addition, J. Eur. Ceram. Soc. 35 (2015) 3835–3841.
[39] M.A. Madre, I. Urrutibeascoa, G. Garcia, M.A. Torres, A. Sotelo, J.C. Diez, High-temperature stability of hot-pressed Sr-doped Ca3Co4O9, J. Electron. Mater. 48 (2019) 1965–1970.
[40] G.J. Snyder, A.H. Snyder, M. Wood, R. Gurunathan, B.H. Snyder, C. Niu, Weighted mobility, Adv. Mater. 32 (2020) 2001537 (Pubmed Partial Author articletitle Page).
[41] Z. Shi, J. Xu, J. Zhu, Y. Zhang, T. Gao, M. Qin, H. Sun, G. Dong, F. Gao, Effect of platelet template seeds on microstructure and thermoelectric properties of Ca3Co4O9 ceramics, Ceram. Int. 45 (2019) 1977–1983.
[42] S. Pinitsoontorn, N. Lerssongkram, N. Keawprak, V. Amornkitbamrung, Thermoelectric properties of transition metals-doped Ca3Co3.8M0.2O9+δ (M = Co, Cr, Fe, Ni, Cu and Zn), J. Mater. Sci. Mater. Electron. 23 (2012) 1050–1056.
[43] J. Rodríguez-Carvajal, Recent advances in magnetic structure determination by neutron powder diffraction, Phys. B Condens. Matter 192 (1993) 55–69.
[44] Y.H. Lin, J. Lan, Z. Shen, Y. Liu, C.W. Nan, J.F. Li, High-temperature electrical transport behaviors in textured Ca3Co4O9-based polycrystalline ceramics, Appl. Phys. Lett. 94 (2009), 072107 (Pubmed Partial Author articletitle stitle Volume Page).
[45] N.F. Mott, H. Jones, The Theory of the Properties of Metals and Alloys, Dover Publications Inc., New York, 1958 (Pubmed Partial Author stitle stitle Volume Page).
[46] N.Y. Wu, T.C. Holgate, N.V. Nong, N. Pryds, S. Linderoth, High temperature thermoelectric properties of Ca3Co4O9+δ by auto-combustion synthesis and spark plasma sintering, J. Eur. Ceram. Soc. 34 (2014) 925–931.
[47] Y. Zhang, J. Zhang, Rapid reactive synthesis and sintering of textured Ca3Co4O9 ceramics by spark plasma sintering, J. Mater. Process. Technol. 208 (2008) 70–74.
[48] D. Flahaut, J. Allouche, A. Sotelo, Sh Rasekh, M.A. Torres, M.A. Madre, J.C. Diez, Role of Ag in textured-annealed Bi2Ca2Co1.7Ox thermoelectric ceramic, Acta Mater. 102 (2016) 273–283.
[49] W. Koshibae, K. Tsuitsui, S. Maekawa, Thermopower in cobalt oxides, Phys. Rev. B 62 (2000) 6869–6872.
[50] M.E. Fine, N. Hsieh, Wiedermann-Franz-Lorenz relation in highly electronic-conducting oxides, J. Am. Ceram. Soc. 57 (1974) 502–503.
[51] D. Kenfaui, B. Lenoir, D. Chateigner, B. Ouladdiaf, M. Gomina, J.G. Noudem, Development of multilayer textured Ca3Co4O9 materials for thermoelectric generators: influence of the anisotropy on the transport properties, J. Eur. Ceram. Soc. 32 (2012) 2405–2414.
[52] R. Tian, T. Zhang, D. Chu, R. Donelson, L. Tao, S. Li, Enhancement of high temperature thermoelectric performance in Bi, Fe co-doped layered oxide-based material Ca3Co4O9+δ, J. Alloys Compd. 615 (2014) 311–315.
[53] I.V. Matsukevich, A.I. Klyndyuk, E.A. Tugova, A.N. Kovalenko, A.A. Marova, N. S. Krasutskaya, Thermoelectric properties of Ca3-xBixCo4O9+δ ($0.0 \leq x \leq 1.5$) ceramics, Inorg. Mater. 52 (2016) 593–599.
[54] A.I. Klyndyuk, I.V. Matsukevich, Synthesis and properties of Ca2.8Ln0.2Co4O9+δ (Ln = La, Nd, Sm, Tb, Er) solid solutions, Inorg. Mater. 48 (2012) 1052–1057.
[55] C.J. Engberg, E.H. Zehms, Thermal expansion of Al2O3, BeO, MgO, B4C, SiC, and TiC above 1000°C, J. Am. Ceram. Soc. 42 (1959) 300–305.
[56] A.K. Krolicka, M. Piersa, A. Mirowska, M. Michalska, Effect of sol-gel and solid-state synthesis techniques on structural, morphological and thermoelectric performance of Ca3Co4O9, Ceram. Int. 44 (2018) 13736–13743.
[57] F. Delorme, P. Diaz-Chao, F. Giovannelli, Effect of Ca substitution by Fe on the thermoelectric properties of Ca3Co4O9 ceramics, J. Electroceram. 40 (2018) 107–114.
[58] N. Wu, T.C. Holgate, N.V. Nong, N. Pryds, S. Linderoth, Effects of synthesis and spark plasma sintering conditions on the thermoelectric properties of Ca3Co4O9 +δ, J. Electron. Mater. 42 (2013) 2134–2142.
[59] S. Butt, Y.-C. Liu, J.-L. Lan, K. Shehzad, B. Zhan, Y. Lin, C.-W. Nan, High-temperature thermoelectric properties of La and Fe co-doped Ca–Co–O misfit-layered cobaltites consolidated by spark plasma sintering, J. Alloys Compd. 588 (2014) 277–283.
[60] P. Mele, H. Kamei, H. Yasumune, K. Matsumoto, K. Miyazaki, Development of thermoelectric module based on dense Ca3Co4O9 and Zn0.98Al0.02O legs, Met. Mater. Int. 20 (2014) 389–397.